Structural and Electrical Investigation of Oxide Ion and Proton Conducting Titanium Cuspidines

M. C. Martín-Sedeño,[†] D. Marrero-López,[‡] E. R. Losilla,[†] L. León-Reina,[†] S. Bruque,[†]
P. Núñez,[‡] and M. A. G. Aranda*,[†]

Departamento de Química Inorgánica, Universidad Málaga, 29071 Málaga, Spain, and Departamento de Química Inorgánica, Universidad La Laguna, 38200 La Laguna, Tenerife, Spain

The $La_4(Ga_{2-x}Ti_xO_{7+x/2}\square_{1-x/2})O_2$ ($x = 0-2$) cuspidine series has been prepared as single phases in the full compositional range. The evolution of the cell parameters is smooth along the series although the symmetry changes from monoclinic $P2_1/c$ for $La_4(Ga_2O_7\square_1)O_2$ to orthorhombic *Pnam* for $La_4(Ti_2O_8)O_2$. The crystal structure of $La_4(Ga_1Ti_1O_{7.5}\square_{0.5})O_2$ has been determined from a refinement of neutron and laboratory X-ray powder diffraction data at room and high temperatures. This compound crystallizes in the $P2_1/c$ space group, $Z = 4$, with $a = 7.9629(2)$ Å, $b = 11.1000(2)$ Å, $c = 11.8294(4)$ Å, $\beta = 109.689$-(4)°, and $V = 984.44(4)$ Å^3. The neutron Rietveld disagreement factors at room temperature were $R_{WP} = 3.10\%$ and $R_F = 3.36\%$. The Ga^{3+}/Ti^{4+} aliovalent substitution is accompanied by extra oxygen needed for the charge compensation. This oxygen transforms the isolated ditetrahedral groups in $La_4(Ga_2O_7\square_1)$-O_2 into infinite trigonal bipyramid chains with interruptions due to the oxygen vacancies in $La_4(Ga_{1.0}Ti_{1.0}O_{7.5}\square_{0.5})O_2$ and into infinite trigonal bipyramid chains in $La_4(Ti_2O_8)O_2$. The electrochemical characterization under different atmospheres (static air, dry Ar, wet Ar, dry 5% H_2−Ar, and wet 5% H_2−Ar) indicates that there is a significant proton contribution to the overall conductivity below ∼950 K for samples with intermediate compositions. Above that temperature, the conductivities are predominantly due to ion oxide. The ion oxide transport numbers range between 0.99 and 0.93, depending upon the temperature and oxygen partial pressure. Small p- and n-type electronic contributions have been observed by thermal and electrochemical analysis under oxidizing and reducing conditions, respectively.

Introduction

Oxide ion conductors are an important group of materials which have been increasingly studied because of their applications in many devices with high technological interest, such as electrolytes in solid oxide fuel cells (SOFCs), oxygen sensors, electrochemical oxygen pumps, oxygen-permeable membrane catalysts, and so forth. SOFCs are devices that convert chemical energy directly into electricity and promise important advantages in comparison to the current technologies based on the combustion fossil fuels, because they provide electrical power with low emission of pollutants and high energy conversion efficiency.[1−3] The commercial SOFC systems use yttria-stabilized zirconia, YSZ, as the electrolyte, which is a good ionic conductor at high temperature (typically 0.1 S·cm^{-1} at 1273 K). However, the high operation temperatures of YSZ (1073−1273 K) limit the choice of stable materials for SOFC components and increase the production costs. Hence, there are extensive efforts to identify new oxide ion conductors, which may display higher conductivities at lower temperatures.

Several types of oxide ion conductors are being deeply investigated for intermediate-temperature solid oxide fuel cells SOFCs which include principally fluorite-type oxides such as $Ce_{0.8}Gd_{0.2}O_{1.9}$[4] and doped perovskite-type compounds such as $La_{0.9}Sr_{0.1}Ga_{0.8}Mg_{0.2}O_{2.85}$,[5] showing higher conductivities than YSZ at lower temperatures. $La_2Mo_2O_9$-based materials[6−8] and oxy-apatites[9−12] also show high oxide ion conductivity. However, they seem to present some drawbacks such as degradation under reducing conditions, residual electronic conductivity, or high grain boundary resistances that must be studied in depth.

In addition, a new type of ionic conductors based on the cuspidine structure have been recently reported.[13−15] Cus-

* To whom the correspondence should be addressed. E-mail: g_aranda@uma.es.
† Universidad Málaga.
‡ Universidad La Laguna.

(1) Ormerod, R. M. *Chem. Soc. Rev.* **2003**, *32*, 17.
(2) Boudghene Stambouli, A.; Traversa, E. *Renewable Sustainable Energy Rev.* **2002**, *6*, 433.
(3) Steele, B. C. H.; Heinzel, A. *Nature* **2001**, *414*, 345.
(4) Torrens, R. S.; Sammes, N. M.; Tompsett, G. A. *Solid State Ionics* **1998**, *111*, 9.
(5) Ishihara, T.; Matsuda, H.; Takita, Y. *J. Am. Chem. Soc.* **1994**, *116*, 3801.
(6) Lacorre, P.; Goutenoire, F.; Bohnke, O.; Retoux, R.; Laligant, Y. *Nature* **2000**, *404*, 856.
(7) Marrero-López, D.; Ruiz-Morales, J. C.; Nuñez, P.; Abrantes, J. C. C.; Frade, J. R. *J. Solid State Chem.* **2004**, *177*, 2378.
(8) Collado, J. A.; Aranda, M. A. G.; Cabeza, A.; Olivera-Pastor, P.; Bruque, S. *J. Solid State Chem.* **2002**, *167*, 80.
(9) Nakayama, S.; Kageyama, T.; Aono, H.; Sadaoka, Y. *J. Mater. Chem.* **1995**, *5*, 1801.
(10) Islam, M. S.; Tolchard, J. R.; Slater, P. R. *Chem. Commun.* **2003**, 1486; Tolchard, J. R.; Islam, M. S.; Slater, P. R. *J. Mater. Chem.* **2003**, *13*, 1956.
(11) León-Reina, L.; Martín-Sedeño, M. C.; Losilla, E. R.; Cabeza, A.; Martínez-Lara, M.; Bruque, S.; Marques, F. M. B.; Sheptyakov, D. V.; Aranda, M. A. G. *Chem. Mater.* **2003**, *15*, 2099.
(12) León-Reina, L.; Losilla, E. R.; Martínez-Lara, M.; Bruque, S.; Aranda, M. A. G. *J. Mater. Chem.* **2004**, *14*, 1142.
(13) Joubert, O.; Magrez, A.; Chesnaud, A.; Caldes, M. T.; Jayaraman, V.; Piffard, Y.; Brohan, L. *Solid State Sci.* **2002**, *4*, 1413.
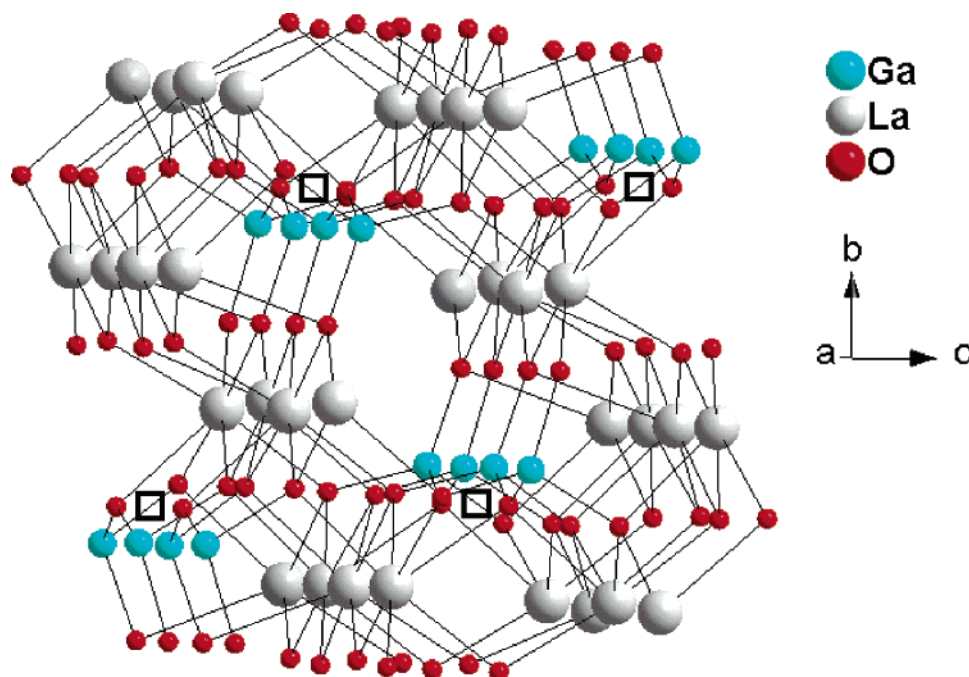
Figure 1. Ball and stick crystal structure of $La_4(Ga_{2.0}O_{7.0}\square_{1.0})O_2$. The positions of the oxygen vacancies, $\square$, are highlighted.

pidines form a family of compounds with the general formula $A_4(Si_2O_7)X_2$ (A = divalent cation; X = OH, F, O). The archetypal member of this family is $Ca_4(Si_2O_7)(OH,F)_2$[16] which crystallizes in the space group $P2_1/c$. The cuspidine structure is well-known, and its framework can be described as built up of chains of edge-sharing AO_7/AO_8 polyhedra running parallel to the a axis with tetrahedral disilicate groups, Si_2O_7, interconnecting these ribbons through the vertexes. The structural formula of cuspidine is better written as $Ca_4(Si_2O_7\square_1)(OH,F)_2$ to directly show the vacant position between the disilicate groups. Several oxy-cuspidine materials are known, such as $Eu_4(Al_2O_7\square_1)O_2$,[17] $Y_4(Al_2O_7\square_1)O_2$,[18,19] $Pr_4(Ga_2O_7\square_1)O_2$,[20] and $La_4(Ga_2O_7\square_1)O_2$.[14] The crystal structure of $La_4(Ga_2O_7\square_1)O_2$ is shown in Figure 1, and the positions of the oxygen vacancies have been highlighted. The filling of that position converts the isolate pyrogroups into infinite chains of distorted trigonal bipyramids.[13] $Ln_4(Ti_2O_8)$-O_2 (Ln = La, Y, Nd, Eu),[21–24] commonly formulated as Ln_2-TiO_5, contains such infinite chains.

The oxide conductivity properties of $La_4(Ga_2O_7\square_1)O_2$ have been optimized by substitution of Ga^{3+} by Ge^{4+}. This aliovalent doping induces a concomitant filling of some

oxygen vacancies which resulted in an enhancement of the ionic conductivity with a maximum value for $La_4(Ga_{1.4}$-$Ge_{0.6}O_{7.3}\square_{0.7})O_2$ and with negligible electronic conductivity, even under very reducing conditions.[14] The oxide ion conductivity for the analogous $Nd_4(Ga_2O_7\square_1)O_2$ compound has also been studied and optimized by partial substitution of Ga^{3+} by Ge^{4+} and Ti^{4+}.[13,15] The Ge^{4+} substitution led to higher oxide conductivities than that obtained by the Ti^{4+} substitution.

In this work, we have carried out a thorough study to evaluate the influence of Ti^{4+} substitution on the structure and transport properties of $La_4(Ga_2O_7\square_1)O_2$. The oxygen-variable $La_4(Ga_{2-x}Ti_xO_{7+x/2}\square_{1-x/2})O_2$ series has been prepared as single phases in the full compositional range ($x = 0-2$). These compounds have been investigated by neutron diffraction to describe the crystal structures, including the oxygen sublattice. The electrochemical characterization surprisingly shows that both oxide and proton conductivities take place for intermediate compositions.

Experimental Section

Synthesis. The series $La_4(Ga_{2-x}Ti_xO_{7+x/2}\square_{1-x/2})O_2$ ($x = 0.0, 0.3,$ $0.7, 1.0, 1.3, 1.7,$ and 2.0) was prepared by the ceramic method using high purity oxides: La_2O_3 (Alfa, 99.999%), Ga_2O_3 (Alfa, 99.99%), and activated TiO_2. Lanthanum oxide was preheated at 1273 K for 2 h to achieve decarbonation. Activated TiO_2 was prepared by slow hydrolysis of commercial $Ti(OCH(CH_3)_2)_4$ with a 1:4 water-to-propanol solution. The resulting white suspension was centrifuged, washed with water, and heated at 573 K for 24 h. Part of this sample was heated at 1273 K to determine the small weight loss due to the residual water. This loss was taken into account when preparing the reagent mixtures. The precursors, in the stoichiometric amounts to prepare 5 g of sample, were mixed in an agate mortar for 10 min and heated at 1473 K for 12 h by the following overall reaction:

$$2La_2O_3 + [(2-x)/2]Ga_2O_3 + xTiO_2 \xrightarrow{\Delta} La_4(Ga_{2-x}Ti_xO_{7+x/2})O_2$$
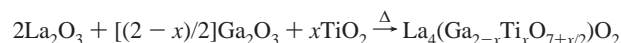
(14) Martín-Sedeño, M. C.; Losilla, E. R.; León-Reina, L.; Bruque, S.; Marrero-López, D.; Núñez, P.; Aranda, M. A. G. *Chem. Mater.* **2004**, *16*, 4960–4968.
(15) Chesnaud, A.; Joubert, O.; Caldes, M. T.; Gosh, S.; Piffard, Y.; Brohan, L. *Chem. Mater.* **2004**, *16*, 5372.
(16) Saburi, S.; Kawahara, A.; Henmi, C.; Kusachi, I.; Kihara, K. *Mineral. J.* **1977**, *8*, 286.
(17) Brandle, C. D.; Steinfink, H. *Inorg. Chem.* **1969**, *8*, 1320.
(18) Christensen, A. N.; Hazell, R. G. *Acta Chem. Scand.* **1991**, *45*, 226.
(19) Yamane, H.; Shimada, M.; Hunter, B. A. *J. Solid State Chem.* **1998**, *141*, 466.
(20) Gesing, Th. M.; Uecker, R.; Buhl, J. C. *Z. Kristallogr.* **1999**, *214*, 431
(21) Bertaud, E. F.; Guillem, M. *Bull. Soc. Fr. Ceram.* **1966**, *72*, 57.
(22) Mumme, W. G.; Wadsley, A. D. *Acta Crystallogr.* **1968**, *24*, 1327.
(23) Müller-Buschbaum, H.; Scheunemann, K. *J. Inorg. Nucl. Chem.* **1973**, *35*, 1091.
(24) Müller-Buschbaum, H.; Werner, J. P. *J. Alloys Compd.* **1994**, *206*, L11.

After cooling, the samples were milled for 3 h in a Fritsch ball mill (model Pulverisette 7, 45 cm³ agate vessel containing seven agate balls with a diameter of 15 mm) at 100 rpm with reverse rotation every 20 min, pelletized at 100 MPa, and heated at 1673 K for 48 h in ZGS−Pt−10% Rh crucibles. The samples were slowly cooled to room temperature (RT) to obtain an oxygen content as close as possible to equilibrium. The samples are hereafter labeled as Ti$_x$ for the La$_4$(Ga$_{2-x}$Ti$_x$O$_{7+x/2}$□$_{1-x/2}$)O$_2$ (x = 0.0 0.3, 0.7, 1.0, 1.3, 1.7, and 2.0) series.

Powder Diffraction. All samples were characterized by laboratory X-ray powder diffraction (LXRPD) at RT. The powder patterns were collected on a Siemens D5000 automated diffractometer, using graphite-monochromated Cu Kα$_{1,2}$ radiation. The samples were loaded in flat aluminum holders and scanned between 10 and 100° (2θ) in 0.03° steps, counting 16 s per step. Full structural characterization was carried out for Ti$_{1.0}$ and Ti$_{2.0}$ by a combined analysis of LXRPD and neutron powder diffraction (NPD) at RT. Crystal structures at high temperature have been derived exclusively from the NPD data for Ti$_{1.0}$. All Rietveld[25] analyses were done using the GSAS suite of programs.[26]

NPD data for Ti$_{1.0}$ and Ti$_{2.0}$ compositions were collected on a HRPT diffractometer [SINQ neutron source at Paul Scherrer Institut, Villigen, Switzerland] with the sample loaded in a vanadium can. High-temperature neutron powder diffraction (HT-NPD) data for Ti$_{1.0}$ were collected at 1073 K under vacuum. The HRPT was used in the "medium-resolution" mode with a wavelength of ∼1.886 Å which was selected by the vertically focusing (511) Ge monochromator. The overall measuring time was ∼8 h per pattern to have good statistics over the 2θ angular range of 5−165° [21−0.95 Å] with a 0.05° step size. Quick patterns were collected on heating each 100 K to determine the thermal expansion coefficients for Ti$_{1.0}$.

Finally, high-resolution LXRPD patterns were collected for two samples in a Philips X'Pert Pro automated diffractometer, equipped with a Ge(111) primary monochromator and a X'celerator detector. The scans were performed in high-resolution mode, 2θ range from 10 to 60°, using strictly monochromatic Cu Kα$_1$ radiation. The studied materials were as-prepared Ti$_{1.0}$ and vibratory milled Ti$_{1.0}$. This last sample was prepared as described below to obtain dense pellets for the electrical characterization.

Microstructural Characterization. The sintered pellets morphology was studied using a JEOL JSM-6300 scanning electron microscope. The pellet surfaces were polished with diamond paste and thermally etched at 50 K below the sintering temperature for 15 min. Finally, the samples were metallized by gold sputtering for better image definition.

Thermal Analysis. Thermogravimetric differential thermal analyses (TG-DTA) were performed for all compositions on a Pyris-Diamond Perkin-Elmer apparatus. The temperature was varied from RT up to 1073 K at a heating/cooling rate of 10 K·min⁻¹ with a flux of air of 80 cm³·min⁻¹, using a mass around 60−70 mg. The TG-DTA instrument was calibrated using standard samples, and the baseline was corrected.

Different heating/cooling cycles were carried out to study the thermal reversibility and reproducibility of the measurements. Thermomechanical analysis was performed for Ti$_{1.0}$ on a NETZSCH Gerätebau 402 EP apparatus. The temperature was varied from RT up to 1273 K at a heating rate of 5 K·min⁻¹ with a silica support on a 3 mm long specimen with a residual porosity of 12%.

Electrical Measurements. Electrical characterization was carried out on cylindrical pellets (∼10 mm diameter and ∼1 mm thickness) obtained by pressing ∼0.3 g of sample with small average particle size [d_{50} ∼ 3 μm] at 125 MPa, for 5 min. The pellets were sintered at 1723 K for 4 h at a heating rate of 5 K·min⁻¹. Fine powders of each composition were obtained by grinding the initial powdered sample in a vibratory ball mill (Retsch, two zircona balls with a diameter of 12.25 mm and a vessel volume of 8 cm³) at 20 Hz for 12 min. The optimum milling time was selected measuring the particle/agglomerate size distribution after different grinding times on a Coulter LS130 laser diffraction analyzer. Electrodes were made by coating opposite pellet faces with METALOR 6082 platinum paste and heating to 1223 K at a rate of 10 K·min⁻¹ for 15 min in air to decompose the paste and to harden the Pt residue. Successive treatments were made to achieve an electrical resistance of both pellet faces lower than 1 Ω.

Impedance spectroscopy data in static air and four different flowing atmospheres (dry Ar, wet Ar, dry 5% H$_2$−Ar, and wet 5% H$_2$−Ar) were collected using a Solartron 1260 frequency response analyzer over the frequency range from 0.1 Hz to 1 MHz. The applied voltage was 200 mV in the temperature range of 1273−673 K and 250 mV between 623 and 573 K. Electrical measurements were taken on heating and cooling processes every 50 K (accuracy of ±1 K) at 5 K·min⁻¹. A delay time of 20 min at each temperature was selected to ensure thermal stabilization. Measurements were electronically controlled by the Zplot program.

High-temperature conductivity measurements as a function of oxygen partial pressure [$p(O_2)$ from air to ∼10⁻²⁰ atm] were performed in a closed tube furnace cell. The $p(O_2)$ values were monitored by using a YSZ oxygen sensor, placed next to the pellet in the cell. The conductivity was continually recorded as a function of $p(O_2)$. The process consists of flushing the system with a dry 5% H$_2$−Ar gas mixture for 12 h at 1173 K to reach a minimum in oxygen activity inside the furnace and to ensure complete reduction of the sample. After that, the oxygen partial pressure was slowly raised back to atmospheric pressure by free diffusion, because the system is not airtight. Each isothermal cycle took over 48 h to complete.

The electronic conductivity was determined by a modified electromotive force (emf) method, taking into account electrode polarization.[27,28] This modification of the classical emf technique eliminates possible errors in the determination of ion transference numbers, arising as a result of electrode polarization. These errors are not negligible for electrolyte materials which have relatively low electronic conductivity.[28,29] The ionic transport numbers t_o were measured under a $p(O_2)$ gradient of pure O$_2$/air and dry/wet 5% H$_2$−Ar/air, using a continuous flux of these gases in the temperature range of 973−1173 K. A YSZ tube was used to measure the theoretical emf under these conditions, E_{th}. The emf observed in the sample, E_{obs}, was measured with an external variable resistance R_M, in parallel to the measuring cell, varying from 10 to 20 kΩ. Experimental data were fitted with the equivalent circuit proposed by Gorelov.[27] In this case, the ionic resistance R_o, the electronic resistance R_e, and the polarization resistance R_η are related to the emf values (E_{th} and E_{obs}) from the relation

$$\frac{E_{th}}{E_{obs}} - 1 = (R_o + R_\eta)\left[\frac{1}{R_e} + \frac{1}{R_M}\right]$$

The dependence of (E_{th}/E_{obs}) − 1 versus $1/R_M$ is a linear plot with slope $R_o + R_\eta$, and the interception over the $1/R_M$ axis is equal

(25) Rietveld, H. M. *J. Appl. Crystallogr.* **1969**, *2*, 65.
(26) Larson, A. C.; von Dreele, R. B. *GSAS program*; Los Alamos National Lab. Rep. No. LA-UR-86748; Los Alamos National Laboratory: Los Alamos, NM, 1994.

(27) Gorelov, V. P. *Elektrokhimiya* **1988**, *24*, 1380.
(28) Mazorau, I. P.; Marrero-López, D.; Azula, A. L.; Kharton, V. V.; Tsipis, E. V.; Núñez, P.; Frade, J. *Electrochim. Acta* **2004**, *49*, 3517.

Table 1. Unit Cell Parameters and Disagreement Factors for the La$_4$(Ga$_{2-x}$Ti$_x$O$_{7+x/2}$□$_{1-x/2}$)O$_2$ (x = 0, 0.3, 0.7, 1.0, 1.3, 1.7, and 2.0) Series from Rietveld Refinements

	space group	a (Å)	b (Å)	c (Å)	β/α (deg)	V/Z (Å^3)	R_{wp}^X/R_{wp}^N (%)	R_F^X/R_F^N (%)
La$_4$(Ga$_2$O$_7$□$_1$)O$_2$[a] [from ref 14]	$P12_1/c1$	7.9768(1)	11.2036(2)	11.6257(2)	109.460(1)	245.04(1)	8.44/1.55	2.09/0.79
La$_4$(Ga$_{1.7}$Ti$_{0.3}$O$_{7.15}$□$_{0.85}$)O$_2$[b]	$P12_1/c1$	7.9804(2)	11.1660(2)	11.7101(5)	109.916(6)	245.27(1)	7.92/−	2.40/−
La$_4$(Ga$_{1.3}$Ti$_{0.7}$O$_{7.35}$□$_{0.65}$)O$_2$[b]	$P12_1/c1$	7.9748(2)	11.1369(4)	11.7683(9)	109.81(1)	245.83(1)	8.79/−	3.28/−
La$_4$(Ga$_{1.0}$Ti$_{1.0}$O$_{7.5}$□$_{0.5}$)O$_2$ RT[a,c]	$P12_1/c1$	7.9629(2)	11.1000(2)	11.8294(4)	109.689(4)	246.11(1)	9.44/3.10	3.07/3.36
La$_4$(Ga$_{1.0}$Ti$_{1.0}$O$_{7.5}$□$_{0.5}$)O$_2$ 1073 K[d]	$P12_1/c1$	8.0047(3)	11.1123(5)	11.8456(8)	109.788(8)	247.87(2)	−/3.28	−/3.81
La$_4$(Ga$_{0.7}$Ti$_{1.3}$O$_{7.65}$□$_{0.35}$)O$_2$[b]	$P2_1/n11$	11.1056(3)	11.1571(3)	3.9814(1)	89.99(1)	246.66(1)	9.58/−	3.21/−
La$_4$(Ga$_{0.3}$Ti$_{1.7}$O$_{7.85}$□$_{0.15}$)O$_2$[b]	$P2_1/n11$	11.0621(3)	11.2657(3)	3.9668(1)	89.99(1)	247.17(1)	11.87/−	3.64/−
La$_4$(Ti$_2$O$_8$)O$_2$[a]	$Pnam$	11.0092(2)	11.4063(2)	3.9433(1)	90.00	247.60(1)	11.22/4.16	2.77/2.26

[a] Joint LXRPD and NPD data refinement. [b] LXRPD data refinement. [c] The refinement in $P2_1/n11$ converged to a=11.1007(3) Å, b = 11.1384(3) Å, c = 3.9818(1) Å, α = 89.986(6)°, V/Z = 246.15(1) Å^3, R_{WP}^X = 9.91%, R_{WP}^N = 3.27%, R_F^X = 2.98%, and R_F^N = 3.11%. [d] NPD data refinement.

to $-1/R_e$. The total resistance R_T was determined independently by impedance spectra data. Ionic transport numbers were calculated as $t_o = 1 - R_T/R_e$.

Results and Discussion

Synthesis and Crystal Structures. The La$_4$(Ga$_{2-x}$Ti$_x$O$_{7+x/2}$□$_{1-x/2}$)O$_2$ (x = 0.0, 0.3, 0.7, 1.0, 1.3, 1.7, and 2.0) series has been prepared as highly crystalline compounds. All compositions were single phases, showing that a full solid solution can be obtained with the cuspidine-type structure for the Ga^{3+}/Ti^{4+} aliovalent substitution. The unit cell parameters derived from the Rietveld refinements for all compositions are given in Table 1. The volume increases with x (see Table 1) as the substitution of Ga^{3+} by Ti^{4+} is accompanied by the introduction of extra oxygen in the empty position to balance the charges.

At this point it is worth highlighting that the structure along this series changes from monoclinic $P2_1/c$, with a unit cell volume of 980.1 Å^3 (Z = 4), for La$_4$(Ga$_2$O$_7$□$_1$)O$_2$ to orthorhombic $Pnam$, with a unit cell volume of 495.2 Å^3 (Z = 2), for La$_4$(Ti$_2$O$_8$)O$_2$. The structural relationship between both structures has been recently pointed out,[13] and the filling of the oxygen vacancy (see Figure 1) changes the symmetry from monoclinic $P12_1/c1$ to monoclinic (pseudo-orthorhombic) $P2_1/n11$ (with half a axis and $\alpha \sim 90.0°$) and, finally, to orthorhombic $Pnam$.

The crystal structures of the end members of the series are already known. The structure of La$_4$(Ga$_2$O$_7$□$_1$)O$_2$ was recently derived from a joint Rietveld refinement of NPD and LXRPD data.[14] The structure of La$_4$(Ti$_2$O$_8$)O$_2$ was reported in 1966,[30] and we have reanalyzed its structure to ensure the symmetry and to obtain accurate atomic parameters. To do so, the RT joint Rietveld refinement of NPD and LXRPD data was carried out using the previous reported structure[30] (orthorhombic $Pnam$) and also in the nonstandard monoclinic $P2_1/n11$ symmetry. The final fit for the orthorhombic description was very good, and the unit parameters and the Rietveld disagreement factors are given in Table 1. The refined atomic parameters and the La−O bond distances are given in Supporting Information as Tables S1 and S3, respectively. The Ti−O bond distances and angles are given in Table 2. The final fit in the monoclinic symmetry is quite

(29) Kharton, V. V.; Viskup, A. P.; Figueiredo, F. M.; Naumovich, E. N.; Yaremchenko, A. A.; Marques, F. M. B. *Electrochim. Acta* **2001**, *46*, 2879.

(30) Guillen, M.; Bertaut, E. F. *C. R. Acad. Sci.* **1966**, *262*, 962.

Table 2. M−O (M = Ga, Ti) Bond Lengths (Å) and Angles (deg) for La$_4$(Ga$_1$Ti$_1$O$_{7.5}$□$_{0.5}$)O$_2$ at RT and 1073 K and La$_4$(Ti$_2$O$_8$)O$_2$ at RT

	Ti$_{1.0}$ RT[a]	Ti$_{1.0}$ 1073 K[b]	Ti$_{2.0}$ RT[a]
M(1)−O(2)	1.80(2)	1.71(5)	1.895(4)
M(1)−O(3)	1.88(2)	1.87(4)	2.031(1) × 2
M(1)−O(4)	1.84(2)	1.95(5)	1.883(4)
M(1)−O(5)[c]	2.07(3)	2.37(5)	1.760(4)
M(1)−O(10)[c]	1.83(3)	1.70(7)	
⟨M(1)−O⟩	1.88	1.92	1.920
M(2)−O(1)	1.93(2)	2.15(5)	
M(2)−O(5)[c]	1.87(2)	2.38(6)	
M(2)−O(6)	1.82(2)	1.73(5)	
M(2)−O(7)	1.62(2)	1.53(5)	
M(2)−O(10)[c]	2.49(2)	1.96(8)	
⟨M(2)−O⟩	1.92	1.93	
O(2)−M(1)−O(3)	102.0(10)	104.3(22)	85.8(1) × 2
O(2)−M(1)−O(4)	135.8(10)	126.4(25)	137.1(2)
O(2)−M(1)−O(5)	85.3(11)	81.0(18)	117.0(2)
O(2)−M(1)−O(10)	81.3(10)	88.9(25)	
O(3)−M(1)−O(3)			152.7(2)
O(3)−M(1)−O(4)	121.1(1)	119.2(24)	84.1(1) × 2
O(3)−M(1)−O(5)	95.3(12)	85.0(18)	103.7(1) × 2
O(3)−M(1)−O(10)	109.5(13)	119.3(27)	
O(4)−M(1)−O(5)	81.9(11)	73.7(17)	105.9(2)
O(4)−M(1)−O(10)	92.0(12)	95.2(22)	
O(5)−M(1)−O(10)	153.7(9)	155.4(27)	
O(1)−M(2)−O(5)	88.4(8)	72.6(16)	
O(1)−M(2)−O(6)	123.9(10)	115.2(25)	
O(1)−M(2)−O(7)	108.7(10)	106.1(25)	
O(1)−M(2)−O(10)	75.2(8)	78.0(22)	
O(5)−M(2)−O(6)	94.6(9)	76.9(22)	
O(5)−M(2)−O(7)	113.9(11)	86.7(24)	
O(5)−M(2)−O(10)	146.5(8)	139.1(28)	
O(6)−M(2)−O(7)	120.6(11)	128(4)	
O(6)−M(2)−O(10)	72.1(8)	90.9(24)	
O(7)−M(2)−O(10)	99.2(9)	129.1(30)	
M(1)−O(5)−M(2)	155.8(8)	163.0(18)	
M(1)−O(10)−M(2)	144.4(8)	132.2(25)	
M(1)−O(3)−M(2)			152.3(2)

[a] Joint LXRPD and NPD refinement. [b] NDP refinement. [c] Partially occupied site.

similar with R_{WP}^N and R_{WP}^X values of 4.17 and 11.43%, respectively, and α = 90.003(6)°. Hence, this structural description does not improve the results, and it is not reported here.

The crystal structure of La$_4$(Ga$_1$Ti$_1$O$_{7.5}$□$_{0.5}$)O$_2$ at RT has also been obtained from a joint refinement of the NPD and LXRPD data using the structure of La$_4$(Ga$_{1.4}$Ge$_{0.6}$O$_{7.3}$□$_{0.3}$)O$_2$ (space group $P12_1/c1$) as the starting model, replacing Ge^{4+} by Ti^{4+} and by changing the occupation factors to their nominal values which were refined later. The occupation factors of O(5) and O(10), which join the trigonal bipyramid chains, were freely refined giving 0.79(3) and 0.75(3), respectively. The occupation factors of the two Ga/Ti sites were also refined but constrained to full occupancy of each
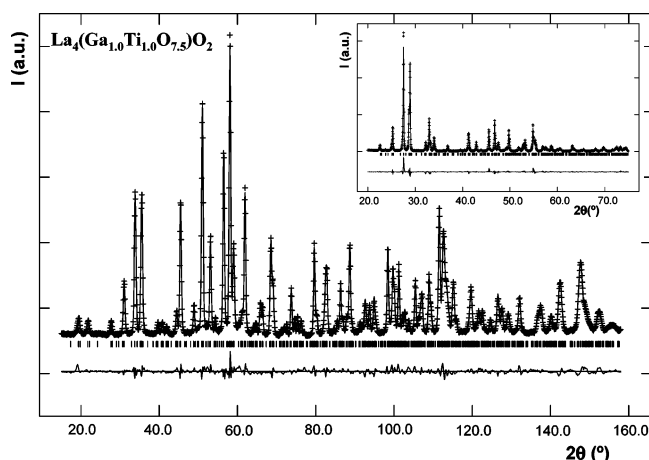
Figure 2. Observed (crosses), calculated (solid line), and difference (bottom) RT-NPD patterns for $La_4(Ga_1Ti_1O_{7.5}\square_{0.5})O_2$. The vertical bars are the allowed Bragg reflections in the $P2_1/c$ space group. The inset shows a selected region $(20-75°/2\theta)$ of the RT-LXRPD Rietveld plot for the same composition.

site. The refined crystallographic stoichiometry was $La_4(Ga_{0.99(2)}Ti_{1.01(2)}O_{7.54(6)})O_2$, which is in excellent agreement with the nominal stoichiometry $La_4(Ga_1Ti_1O_{7.5}\square_{0.5})O_2$. The temperature factors of O(5) and O(10) were constrained to be the same to avoid correlations in the refinements. The final Rietveld disagreement factors are given in Table 1. The refined atomic parameters and the La−O bond distances are given in Supporting Information as Tables S2 and S3, respectively. The Ti−O bond distances and angles are given in Table 2. The Rietveld fits of the neutron and X-ray data are displayed in Figure 2.

We have also carried out the joint Rietveld refinement of the NPD and LXRPD data of the $Ti_{1.0}$ sample in space group *Pnam*. This fit is worse as R_{WP}^N and R_{WP}^X increase from 3.10 and 9.44% to 3.45 and 9.93%, respectively. The structural description in $P2_1/n11$ has also been tested. The unit cell parameters and the Rietveld disagreement factors are also given in Table 1. In this case, the R_{WP} values are only slightly worse ($R_{WP}^N = 3.27\%$, $R_{WP}^X = 9.91\%$) than those obtained in the monoclinic symmetry with the double unit cell axis along the Ti/Ga−O chains; see Table 1. However, the oxygen ordering pattern in the chains is very complex as previously demonstrated for similar materials by high-resolution transmission electron microscopy.[15] So, the structural description reported here should be taken as an average structure which likely contains short-range modulations in the oxygen distribution along the Ga^{3+}/Ti^{4+} chains. Finally, the LXRPD patterns for the $Ti_{1.3}$ and $Ti_{1.7}$ samples have been refined in the $P2_1/n11$ symmetry (see Table 1), but NPD data are needed to validate this point.

The insertion of oxygen into the vacant position, O(10), and the partial emptying of O(5) in the $La_4(Ga_{2-x}Ti_xO_{7+x/2}\square_{1-x/2})O_2$ series equalize the two different distances initially present in the digallate groups and between them, respectively. So, the isolated tetrahedral digallate groups present in $La_4(Ga_2O_7\square_1)O_2$ are converted to infinite bipyramid chains in $La_4(Ti_2O_8)O_2$, with some interruptions due to partial occupancy of both oxygens in $La_4(Ga_1Ti_1O_{7.5}\square_{0.5})O_2$. The Ga/Ti−O and Ti−O bond distance and angle values, Table 2, are typical for these coordination environments.

HT-NPD data were collected for the $Ti_{1.0}$ sample at 1073 K. There is no evidence for any symmetry change. The occupation factors for O(5) and O(10) were also refined freely giving 0.80(5) and 0.66(5), respectively. So, the refined occupation factors of the oxygen in the partially interrupted bipyramid chains do not change significantly on heating. The atomic parameters are given in Table S2. The less strong La−O bond distances increase on heating due to the thermal expansion; see Table S3. However, the shorter Ga/Ti−O bond distances (see Table 2) change little on heating.

The volume thermal expansion coefficient for the $Ti_{1.0}$ sample, derived from NPD data taken each 100 K, was $\alpha_v = 21.6(3) \times 10^{-6}$ K^{-1} [α_v is defined as m/n for the $V(T) = n + mT$(K) fit]. Under the isotropic thermal expansion approximation, the linear expansion coefficient, β_{calc}, can be derived as $\beta_{calc} = \alpha_v/3 = 7.2 \times 10^{-6}$ K^{-1}. The result from the dilatometric study for the same material gave a slightly smaller average polycrystalline linear expansion coefficient value, $\beta_{meas} = 4.7 \times 10^{-6}$ K^{-1}. The difference between these two values is likely due to the experimental errors of the techniques.

Electrical Characterization. The sintering conditions for the pellets led to very dense specimens with compactions ranging between 90 and 95% of the theoretical value (taking into account the pellet mass, volume, and the crystallographic density). No weight losses were detected during the sintering process.

Figure 3 shows a scanning electron microscopy (SEM) micrograph for the $Ti_{1.0}$ sample; similar images were obtained for all compositions. The microstructure is well-developed with an average grain size close to 5 μm and low porosity. No indications of liquid phase formation or phase segregations at the grain boundary were found in any of the studied samples. Additionally, no contamination due to the ball-milling process was detected in the sintered pellets.

A representative impedance spectrum for $Ti_{1.0}$ at 773 K is shown in Figure 4a; similar plots were obtained for all compositions. A depressed broad arc is observed in the high-frequency range which is likely due to the presence of both bulk and grain boundary contributions. The spike due to the blocking electrode effect is clearly observed in the low-frequency range. Because it is inclined to the Z' axis at $\approx 30°$, it is likely indicating a partial-blocking electrode response that allows limited diffusion. At higher temperatures (above 823 K) the spike collapses to a semicircular arc, indicating that oxide ions are able to diffuse through the entire thickness of the electrolyte. In summary, the charge carriers seem to be predominantly ion oxide, although complementary electrochemical measurements as conductivity versus oxygen partial pressure are needed to determine other contributions; see below.

A deeper insight into the electrical microstructure of the pellets can be obtained from the spectroscopic plots of the impedance imaginary part, Z'', and the complex electric modulus, M'', versus log(f); see Figure 5. The maxima of both curves are close ($\sim$1 order of magnitude in frequency) which seems to indicate that the impedance peak is associated with the same RC element responsible of the modulus peak; however, the associated capacitances (5.2 pF·cm^{-1} for M''

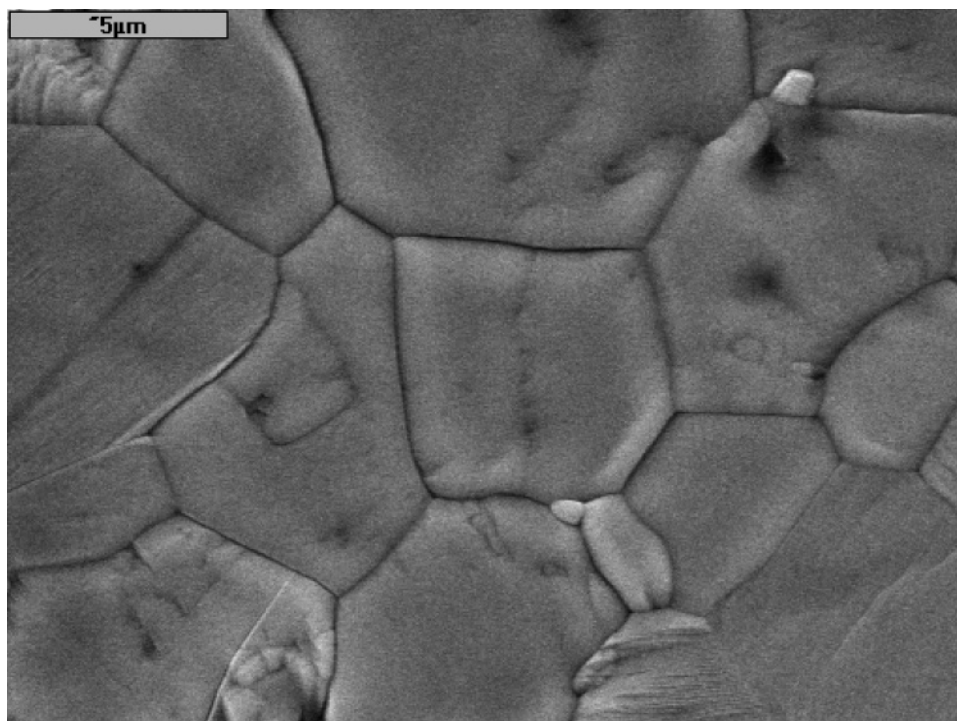**Figure 3.** SEM micrograph of the polished and thermally etched surface for a sintered pellet of $La_4(Ga_1Ti_1O_{7.5}\square_{0.5})O_2$ composition.
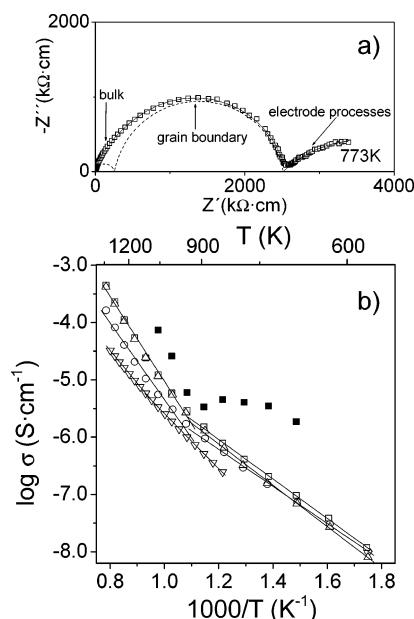

Figure 4. (a) Complex impedance plane plot for $La_4(Ga_{1.0}Ti_{1.0}O_{7.5}\square_{0.5})O_2$ at 773 K in air. The full line is the data fit using the equivalent circuit described in the text. The contribution of each element is also shown separately as a dashed line. (b) Arrhenius plots of log σ for $La_4(Ga_2O_7\square_1)$-O_2 (down triangle), $La_4(Ga_{1.7}Ti_{0.3}O_{7.15}\square_{0.85})O_2$ (circle), $La_4(Ga_{1.0}Ti_{1.0}O_{7.5}\square_{0.5})$-$O_2$ (square), $La_4(Ga_{0.3}Ti_{1.7}O_{7.85}\square_{0.15})O_2$ (up triangle) in air, and log(σ_b) for $La_4(Ga_{1.0}Ti_{1.0}O_{7.5}\square_{0.5})O_2$ (solid square) in air.

and 8.9 pF·cm^{-1} for Z'') are somewhat larger than those expected for a homogeneous bulk value ($\sim$3 pF·cm^{-1} is expected assuming a typical high-frequency permittivity ϵ' of 10–20). Furthermore, the M'' peak shows a shoulder at high frequencies that corresponds to a more conductive element. This relaxation is not well-defined at lower temperatures. To further examine this point, we have plotted the real part of the complex capacitance as a function of frequency (inset of Figure 5). At low frequencies, the
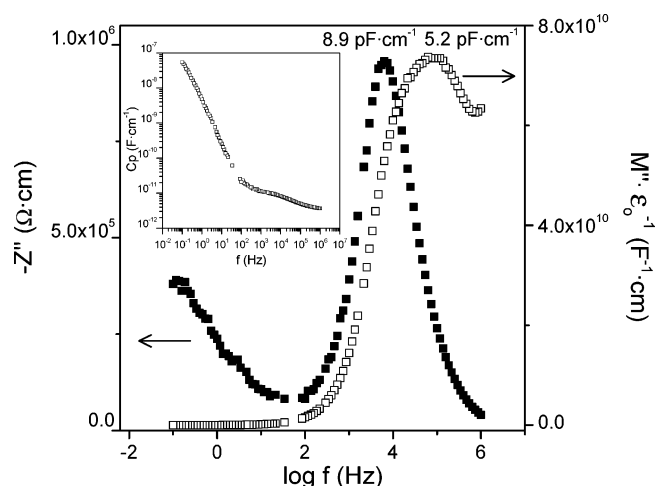

Figure 5. Spectroscopic plots of $-Z''$ and M'' versus log(f) at 773 K for $La_4(Ga_1Ti_1O_{7.5}\square_{0.5})O_2$. The inset shows the real part of the complex capacitance vs frequency at the same temperature.

blocking electrode effect can be observed, and at higher frequencies, the curves show a clear relaxation from $\sim$8 pF·cm^{-1} toward lower values in the pF range as frequency increases. The relaxation, $\sim$8 pF·cm^{-1}, is attributed to a very thick grain boundary or constriction resistance at the region of grain–grain contacts. This component dominates the Z'' spectrum and represents the major part of the total pellet resistance of the samples (R_T).

The total pellet conductivity was obtained from the intercept of the spike (high-frequency end) and/or the broad arc (low-frequency end) on the Z' axis. These values of conductivity were plotted in a traditional Arrhenius format in Figure 4b. A plot of log σ versus $1000/T$ should give a straight line of slope $-E_a/k$ if the activation energy E_a is temperature-independent and only one conduction mechanism takes place. The Arrhenius plots clearly show two
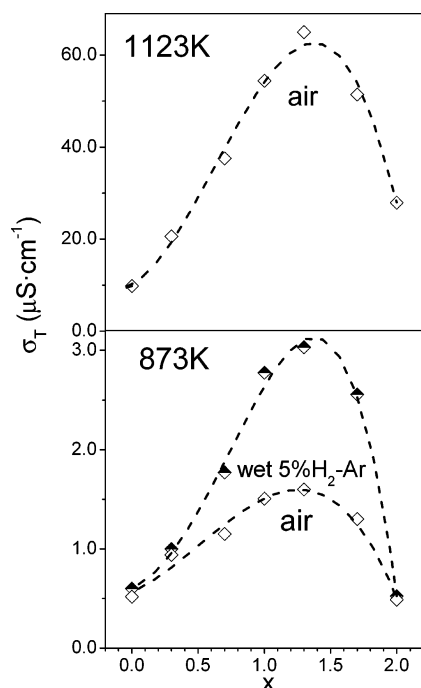
Figure 6. Total conductivities at 873 K under air and wet 5% H_2-Ar (bottom) and at 1123 K under air (top) for all compositions. The dotted lines are guide to the eyes.

Figure 7. TG curves (heating and cooling processes) for $Ti_{2.0}[La_4(Ti_2O_8)\text{-}O_2]$, $Ti_{0.0}[La_4(Ga_2O_7\square_1)O_2]$, $Ti_{1.0}$ as-prepared $[La_4(Ga_1Ti_1O_{7.5}\square_{0.5})O_2 \cdot 0.17H_2O]$, and $Ti_{1.0}$ vibratory ball milled $[La_4(Ga_1Ti_1O_{7.5}\square_{0.5})O_2 \cdot 0.37H_2O]$. All measurements were carried out under dry air flow.

regions with different activation energies. Below ~950 K, the Arrhenius plots for all studied compositions fall on a set of approximately parallel lines with activation energies ranging between 0.70 and 0.72 eV. Above ~950 K, the activation energies increase, ranging between 1.60 and 1.62 eV, except for the $La_4(Ga_2O_7\square_1)O_2$ sample which has a lower value, ~1.01 eV. Some possible explanations for these changes in the activation energy values are (i) a phase transition, but this is ruled out by the HT-NPD study for $La_4(Ga_1Ti_1O_{7.5}\square_{0.5})O_2$; (ii) an enhancement of the grain boundary conductivity at high temperature, although this is not expected because, in general, the grain boundary resistance is small at high temperatures compared to that of the bulk; and (iii) finally, a change in the dominant charge carriers with the temperature. Moreover, it should be noted that the values of activation energies at low temperatures are somewhat lower than those expected for a pure ion oxide conductor (normally between 0.8 and 1.2 eV) which may also suggest a change in the conduction mechanism.

The variation of total conductivity with Ti content (at 873 and 1123 K) under static air is given in Figure 6. These values increase slightly with Ti content, reaching a maximum for the $Ti_{1.3}$ composition. However, higher titanium contents produce a decrease in the total conductivity as the oxygen vacant concentration is reduced in the structure. The total conductivity values at 1123 K were 9.80×10^{-6}, 2.06×10^{-5}, 3.75×10^{-5}, 5.44×10^{-5}, 6.50×10^{-5}, 5.14×10^{-5}, and 2.79×10^{-5} S·cm^{-1} for the $Ti_{0.0}$, $Ti_{0.3}$, $Ti_{0.7}$, $Ti_{1.0}$, $Ti_{1.3}$, $Ti_{1.7}$, and $Ti_{2.0}$ compositions, respectively.

To separate the bulk and grain boundary contributions, complex impedance spectra were analyzed by a nonlinear least-squares fitting method, using equivalent circuits with
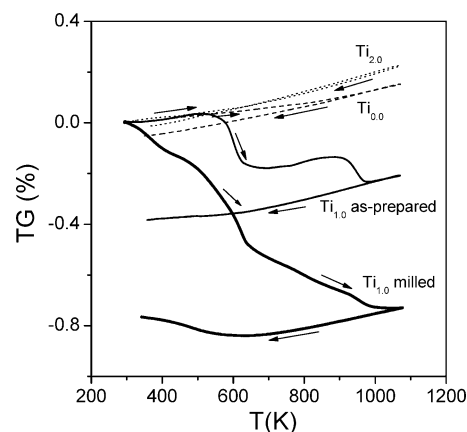
the Zview program.[31] The impedance data have been fitted using an equivalent circuit formed by the association of three (RQ) elements in series: $(R_bQ_b)(R_{gb}Q_{gb})(R_eQ_e)$, corresponding to the bulk, grain boundary, and electrode responses, where R is the resistance in parallel with the pseudocapacitance, Q, which is related to the angular relaxation frequency w_i, and capacitance C_i as follows: $w_i = (R_iC_i)^{-1} = (R_iQ_i)^{(1-n_i)/n_i}$.[32] These parameters have been determined in the 673–1073 K temperature range where the bulk response is detectable. The calculated spectrum at 773 K is shown (solid line) in Figure 4a as an example of the goodness of the fits. These calculations gave the bulk conductivities which are also plotted in the Figure 4b (solid squares) for $Ti_{1.0}$ composition. As it can be seen, there is not a typical Arrhenius behavior, which is another indication of a mixed conduction mechanism. It is also observed that the bulk conductivity is much higher than the total one, indicating the negative effects of the large grain boundary contribution on the total conductivity. To clarify the electrical behavior, the samples were further studied under different atmospheres.

(a) Mixed Ionic (Oxide–Proton) Conductivity. Before further characterization, the samples were heated at 1273 K, slowly cooled at 473 K, and held at this temperature for several hours under air. The IR spectra for the $Ti_{1.0}$ sample obtained after this treatment (not shown) present a weak absorption band at 3500 cm^{-1} characteristic of the O–H stretching vibration.

Four representative cuspidine samples were studied by thermal analysis to characterize the possible incorporation of water. The TG curves for the $La_4(Ga_2O_7\square_1)O_2$ and $La_4(Ti_2O_8)O_2$ samples, taken under dry air flow, are shown in Figure 7, and they do not show any weight loss on heating. Conversely, very slight weight increasing (close to 0.2%) is observed on heating, and this is likely due to very minor oxidation of the samples with the concomitant oxygen uptake. This change is reversible as the oxygen is released on cooling; see Figure 7. These small mass changes are not due

(31) Johnson, D. *ZView*, Version 2.16; software program for IES analysis; Scribner Associates, Inc.: Southern Pines, NC, 2002.
(32) Marrero-López, D.; Canales-Vazquez, J.; Ruiz Morales, J. C.; Irvine, J. T. S.; Núñez, P. *Electrochim. Acta* **2005**, *50*, 4385.

to an improper correction of the baseline. The overall mass variation of the baseline measured with a standard was 0.03%. This study shows that the end members of the reported series do not contain water.

The TG curves for two $Ti_{1.0}$ samples, recorded under dry air flow, are also shown in Figure 7. The as-prepared $Ti_{1.0}$ sample was used in the NPD study, and it was not vibratory ball milled. The second sample, $Ti_{1.0}$ milled, was vibratory ball milled to obtain a dense pellet by decreasing the average particle size. The displayed curves show that superimposed to a small weight increase on heating, also likely due to oxygen uptake, there are large weight losses for both samples. The TG curve for as-prepared $Ti_{1.0}$ shows a weight loss that takes place in two steps centered close to 600 and 950 K. The overall mass lost is close to 0.38%. This number has been obtained by taking into account the mass gain due to the oxygen uptake. During the cooling process, the initial state is not recovered. The weight loss can be due to water absorbed in the sample, which is characteristic of proton conductors. The initial state is not reached in the TG curve because the sample is fluxed with dried air. Under the reasonable assumption that the full weight loss, 0.38%, is due to water release, the overall water content of this sample must be close to $La_4(Ga_1Ti_1O_{7.5}\square_{0.5})O_2\cdot0.17H_2O$.

On the other hand, the TG curve for vibratory milled $Ti_{1.0}$ shows a continuous weight loss up to 1000 K. The overall mass loss, corrected from the oxygen uptake, is close to 0.80%. If this overall mass loss is due to water release, the water content of this sample must be close to $La_4(Ga_1Ti_1O_{7.5}\square_{0.5})O_2\cdot0.37H_2O$. Hence, the water uptake is intrinsic of Ti-doped cuspidines but the amount of water/protons that can be incorporated into the materials depends on the average particle size. Samples with higher surfaces uptake more water.

The main reaction[33,34] for water uptake in oxides is

$$V_{\ddot{o}} + H_2O \rightarrow O_o^x + 2H^+$$
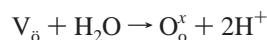
where $V_{\ddot{o}}$ is a vacant site and O_o^x is an oxygen site in the crystal lattice, using the Kröger–Vink notation.[35]

The maximum water uptake according to this would be one water molecule per oxygen vacancy in the cuspidine material. However, water can also be uptaken at the grain boundaries and defects. To investigate this point, we carried out high-resolution powder diffraction study of these two $Ti_{1.0}$ samples with different water contents.

The strictly monochromatic patterns, recorded as described in the experimental section, were analyzed by the Rietveld method to extract the unit cell parameters. All atomic parameters were kept fixed to the values obtained in the NPD study. The refined unit cell parameters obtained for the as-prepared $Ti_{1.0}$ sample (overall chemical formula: $La_4(Ga_1Ti_1O_{7.5}\square_{0.5})O_2\cdot0.17H_2O$) were $a = 7.9656(1)$ Å, $b = 11.1137(2)$ Å, $c = 11.8090(6)$ Å, $\beta = 109.718(6)°$, and $V = 984.13(4)$ Å^3. The unit cell parameters obtained for the
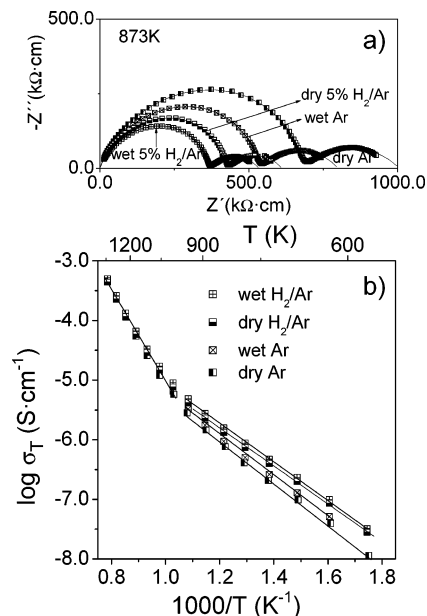

Figure 8. (a) Complex impedance plane plots for $La_4(Ga_1Ti_1O_{7.5}\square_{0.5})O_2$ at 873 K and under different atmospheres. (b) Arrhenius plots of $\log(\sigma_T)$ for the same sample and atmospheres.

vibratory milled $Ti_{1.0}$ sample (overall chemical formula: $La_4(Ga_1Ti_1O_{7.5}\square_{0.5})O_2\cdot0.37H_2O$) were $a = 7.9694(2)$ Å, $b = 11.1217(4)$ Å, $c = 11.8063(9)$ Å, $\beta = 109.73(1)°$, and $V = 984.99(7)$ Å^3. This study shows that the unit cell volume expands 0.09% when the water content increases from $0.17H_2O$ to $0.37H_2O$ per chemical formula. Hence, we can establish that part of the water is absorbed in the crystalline phase. However, from this study we cannot conclude that all uptaken water is retained into the structure and a fraction may be adsorbed at the grain boundaries. Further characterization is planned to address this point. Finally, we have attempted to locate the extra protons (which have negative scattering in neutron diffraction) by difference Fourier maps of the RT NPD pattern for the as-prepared $Ti_{1.0}$ sample. All tests in the $P12_1/c1$ and $P2_1/n11$ space groups were fruitless. So, taking into account that the estimated proton concentration and that $0.17H_2O$ per chemical formula would give a very small but measurable contribution to the overall neutron scattering, we conclude that part of the protons are sorbed in a disordered way.

The water content in the $Ti_{1.0}$ samples and the anomalous electrical behavior suggest a possible proton conductivity mechanism contribution to the total conductivity which was further studied. High-temperature proton conductivity has been reported many times. For example, complex oxides with perovskite structure, such as $BaCeO_3$-based materials[36] and $SrZrO_3$,[37] present proton conductivity in a humidified atmosphere. Hence, an impedance spectroscopy study under different atmospheres was carried out. Figure 8a shows the impedance spectra at 873 K for the $Ti_{1.0}$ sample under constant flow of dry Ar, wet Ar, dry 5% H_2–Ar, and wet 5% H_2–Ar atmospheres. It is obvious from this figure that the sample has the highest conductivity under wet 5% H_2/

(33) Bouwmeester, H. J. M.; Gelling P. J. *The CRC Handbook of Solid State Electrochemistry*; CRC Press: Boca Ratón, 1997.
(34) Norby, T. *Solid State Ionics* **1999**, *125*, 1.
(35) Kröger, F. A.; Vink, H. J. *Solid State Physics* **1956**, *3*, 307.

(36) Iwahara, H.; Uchida, H.; Ono, K.; Ogaki, K. *J. Electrochem. Soc.* **1988**, *135* 529.
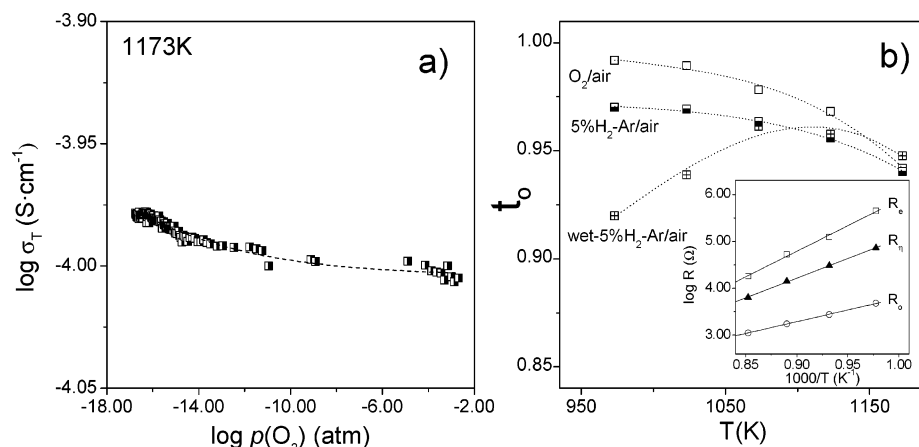(37) Yamija, T.; Susuki, H.; Yogo, T.; Iwahara, H. *Solid State Ionics* **1992**, *51*, 101.

Figure 9. (a) Overall conductivity at 1173 K as a function of oxygen partial pressure for $La_4(Ga_1Ti_1O_{7.5}\square_{0.5})O_2$; (b) dependence of the ion oxide transference number, t_o, for the same sample under oxidizing (O_2/air gradient) and reducing (dry and wet 5% H_2-Ar/air gradient) atmospheres. The inset in part b shows the thermal dependence of overall ionic resistance (R_o), polarization resistance (R_η), and electronic resistance (R_e) under oxidizing conditions.

Ar and the lowest conductivity under dry Ar. The Arrhenius plots of the total conductivity are shown in Figure 8b. Total conductivity increases under humidified atmospheres in the low-temperature range up to 950 K, and almost no conductivity enhancement is observed above this temperature where all data coalesce in the same line.

The impedance results are in very good agreement with the TG results, where there are no mass losses above 1000 K. Hence, above ~950 K, the proton conductivity is negligible (being mainly oxide conductivity, see below), but at lower temperatures its contribution to the overall conductivity is significant and depends on the nature of the atmosphere. At high temperature (i.e., above ~950 K), the activation energy is 1.65 eV which is typical of oxide conductors. In the low-temperature region (i.e., below ~950 K), the activation energy in dry Ar is 0.74 eV and decreases to 0.68 eV in wet 5% H_2-Ar, indicating that the contribution of the proton conductivity is higher in wet atmospheres, as expected. A small electronic contribution in this regime cannot be ruled out, and further electrochemical characterization is needed to establish this point.

Therefore, the curvatures in the Arrhenius plots, Figure 4b, are explained as a consequence of the change in the conduction mechanism from mixed ionic (proton and oxide) below ~950 K to a predominantly oxide above that temperature. Following this study for the $Ti_{1.0}$ sample, impedance data were also collected at 873 K in a wet 5% H_2/Ar atmosphere for all compositions; see Figure 6. The total conductivity values increase with Ti content in the same way under air. However, the end compositions, Ti_0 and $Ti_{2.0}$, do not present significant conductivity enhancement under a wet atmosphere. This is in agreement with the TG results where mass losses, associated to adsorbed water, were not observed. Hence, proton conductivity takes place only for mixed Ga$-$Ti samples with a maximum of proton conductivity for $La_4(Ga_{0.7}Ti_{1.3}O_{7.65}\square_{0.35})O_2$. Furthermore, the non-Arrhenius-type behavior of the bulk conductivities at low temperatures shown in Figure 4b can now be justified. As the temperature increases above 750 K, water starts to be released and the contribution of proton conductivity, to the overall electrical response, diminishes. Above 900 K, the role of the proton conductivity is negligible and an Arrhenius-type behavior

is observed which is predominantly due to oxide ion conductivity.

(b) Mixed Ionic−Electronic Conductivity. The ionic conductivity for a pure ionic conductor is independent of the oxygen partial pressure in a wide range of $p(O_2)$ values. However, the conductivity increases for a mixed ionic−electronic conductor as $p(O_2)$ increases or decreases, depending on the predominant electronic contribution (p- and n-type, respectively). The conductivity data for $Ti_{1.0}$ at 1173 K as a function of $p(O_2)$ are shown in Figure 9a. The conductivity increases slightly as the $p(O_2)$ decreases. It indicates a small n-type contribution under reducing conditions and at high temperature. This temperature was selected because the proton conductivity contribution is negligible.

The dependence of oxide ion transport number (t_o) under oxidizing (O_2/air gradient) and reducing (dry and wet 5% H_2-Ar/air gradient) conditions as a function of temperature is shown in Figure 9b. As it can be observed, the variations of t_o in O_2/air gradient show a slight decreasing from 0.99 at 973 K to 0.95 at 1173 K. This behavior can be ascribed to a small p-type contribution which is associated to oxygen absorption from the air by the sample, according to the following electrochemical reaction:

$$\frac{1}{2}O_2 + V_{\ddot{o}} \leftrightarrow O_o^x + 2h'$$
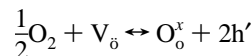
where $V_{\ddot{o}}$ is a vacant site, O_o^x is an oxygen site in the lattice, and h′ is a hole, in the Kröger−Vink notation.[35] The p-type contribution in these samples is in agreement with the TG results, although the study of electronic conductivity as a function $p(O_2)$ under oxidizing conditions, for example, using a faradic efficiency technique, is necessary to confirm this point.

Furthermore, in dry 5% H_2-Ar, the t_o values also decrease with increasing temperature. This behavior is related to a small n-type contribution, previously observed in the $p(O_2)$ measurements, and likely due to a minor Ti^{4+} reduction. In fact, the sample after this treatment became pale pinkish.

On the other hand, the t_o values decrease sharply below 950 K under wet 5% H_2-Ar/air gradient. This feature is ascribed to the appearance of a proton contribution to the

overall conductivity at low temperature, as previously demonstrated. An example of the thermal dependence of R_o, R_η, and R_e is given in the inset of Figure 9b in the O_2/air gradient. The polarization resistance has the same order of magnitude as the electronic one in the studied temperature range. Hence, the electrode polarization has a significant effect, and, therefore, the transport numbers determined by the classical emf method are negatively influenced by the electrode polarization in Ti contained samples.

Conclusions

$La_4(Ga_{2-x}Ti_xO_{7+x/2}\square_{1-x/2})O_2$ compounds with cuspidine structure are oxide conductors at high temperature as previously reported for related materials.[13−15] However, below ∼950 K, in addition to the oxide conductivity, the contribution of proton conductivity is significant and maxi-mum for $La_4(Ga_{0.7}Ti_{1.3}O_{7.65}\square_{0.35})O_2$. Above 1000 K, the oxide ion transport numbers range between 0.99 and 0.93. The electrochemical analysis shows small p- and n-type electronic contributions which have been measured.

Supporting Information Available: Positional parameters for $La_4(Ti_2O_8)O_2$ and $La_4(Ga_1Ti_1O_{7.5}\square_{0.5})O_2$ under various conditions (PDF) as well as crystallographic data (CIF). This material is available free of charge via the Internet at http://pubs.acs.org.

CM051117V